Sparse Ellipsometry: Portable Acquisition of Polarimetric SVBRDF and Shape with Unstructured Flash Photography

INSEUNG HWANG, KAIST, South Korea
DANIEL S. JEON, KAIST, South Korea
ADOLFO MUÑOZ, Universidad de Zaragoza - I3A, Spain
DIEGO GUTIERREZ, Universidad de Zaragoza - I3A, Spain
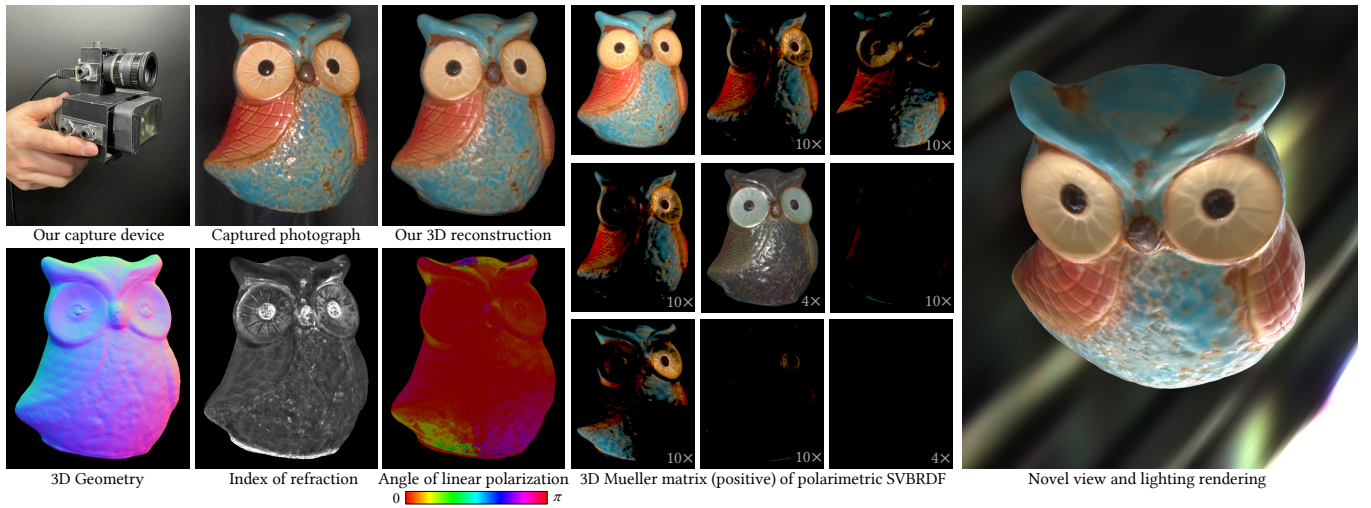XIN TONG, Microsoft Research Asia, China
MIN H. KIM, KAIST, South Korea

Our capture device   Captured photograph   Our 3D reconstruction

3D Geometry   Index of refraction   Angle of linear polarization   3D Mueller matrix (positive) of polarimetric SVBRDF   Novel view and lighting rendering

$0 \qquad \pi$

Fig. 1. We propose the first sparse ellipsometry method that simultaneously captures both the polarimetric SVBRDF (including the *3D Mueller matrix* and the index of refraction) and the 3D shape of real-world objects. Different from traditional ellipsometry, our *portable* acquisition device is made up of off-the-shelf, fixed optical components. Our sparse observations can be captured in minutes instead of days, allowing for accurate renderings of novel views under different illuminations.

Ellipsometry techniques allow to measure polarization information of materials, requiring precise rotations of optical components with different configurations of lights and sensors. This results in cumbersome capture devices, carefully calibrated in lab conditions, and in very long acquisition times, usually in the order of a few days per object. Recent techniques allow to capture polarimetric spatially-varying reflectance information, but limited to a single view, or to cover all view directions, but limited to spherical objects made of a single homogeneous material. We present *sparse ellipsometry*, a portable polarimetric acquisition method that captures both polarimetric SVBRDF and 3D shape simultaneously. Our handheld device consists of off-the-shelf, fixed optical components. Instead of days, the total acquisition time varies between twenty and thirty minutes per object. We develop a complete polarimetric SVBRDF model that includes diffuse and specular components, as well as single scattering, and devise a novel polarimetric inverse rendering algorithm with data augmentation of specular reflection samples via generative modeling. Our results show a strong agreement with a recent ground-truth dataset of captured polarimetric BRDFs of real-world objects.

CCS Concepts: • **Computing methodologies** → **Appearance and texture representations**; **3D imaging**.

Additional Key Words and Phrases: Polarimetric appearance, 3D reconstruction, material appearance, shape

Authors' addresses: Inseung Hwang, KAIST, South Korea, ishwang@vclab.kaist.ac.kr; Daniel S. Jeon, KAIST, South Korea, sjjeon@vclab.kaist.ac.kr; Adolfo Muñoz, Universidad de Zaragoza - I3A, Spain, adolfo@unizar.es; Diego Gutierrez, Universidad de Zaragoza - I3A, Spain, diegog@unizar.es; Xin Tong, Microsoft Research Asia, China, xtong@microsoft.com; Min H. Kim, KAIST, South Korea, minhkim@vclab.kaist.ac.kr.

1 INTRODUCTION

Realistic modeling of the bidirectional reflectance distribution functions (BRDF) of real-world objects is a key aspect for physically based rendering. The effect of scattering on the polarization state of light, however, has been traditionally ignored since it is mostly imperceptible to the human eye. Nevertheless, polarization can be

easily captured by an optical sensor, and provides useful information about the geometry and material properties of an object.

Ellipsometry techniques use optical measurements to characterize how the interactions with a material change the polarization state of incident light [Azzam 2016]. There are two main approaches, represented by two recent works. First, polarimetric spatially-varying reflectance information of real-world objects can be captured, but limited to a single view [Baek et al. 2018]; therefore, changes in viewpoint are not possible without visible distortions. Alternatively, polarimetric information can be measured from all view directions, but limited to spherical objects made of one single, homogeneous material [Baek et al. 2020]. Our work is the first to allow simultaneous capture of both polarimetric spatially-varying materials from all view directions, as well as arbitrary geometry.

Furthermore, while these recent approaches [Baek et al. 2018, 2020] require sophisticated tabletop setups and rotating optical equipment, combining polarization angles with different configurations of light and sensor, we design a portable device that combines an off-the-shelf polarization camera and flashlight with a linear polarizer, without the need for rotating elements. Using our device, we introduce a *sparse ellipsometry* technique that allows us to capture both a complete linear polarimetric spatially-varying BRDF (SVBRDF) and the corresponding 3D geometry of a real-world object from a series of unstructured flash photographs; instead of days as with existing approaches, our method takes only between twenty and thirty minutes of acquisition time, while also yielding an accurate match with ground-truth data.

From the unstructured, sparse set of captured views, we recover polarimetric reflectance and 3D shape using an optimization algorithm that involves inverse rendering. Our polarimetric SVBRDF model includes not only diffuse and specular reflection, but subsurface single scattering as well, accurately matching ground-truth data recently captured with full ellipsometry techniques [Baek et al. 2020]. Since the sparse input data is often insufficient to estimate *per-vertex* specular parameters, specially for very narrow specular lobes, we devise a generative modeling strategy that augments the input with novel synthetic views. Our technique captures linear polarization, which corresponds to the first three components in the Stokes vector. Since we do not capture circular polarization, our scope is restricted to dielectric surfaces.

Figure 1 shows our portable device, along with a captured object, visualization of polarimetric data including the 3D Mueller matrix, and a novel view under different lighting conditions. Note that, even though all the views are captured only with the frontal flash lighting of our device, our inverse rendering technique is robust enough to render captured objects with arbitrary illumination even at grazing angles (see the rightmost image in Figure 1; please refer also to the supplemental video).

In summary, our contributions are:

- A method to capture both polarimetric SVBRDF and 3D geometry information simultaneously.
- A portable measurement device for polarimetric reflectance using off-the-shelf, fixed optics.
- A complete polarimetric SVBRDF model that includes diffuse and specular components, as well as single scattering.

- A polarimetric inverse rendering algorithm that includes a generative modeling strategy for data augmentation.

Our code is freely available for research purposes[1].

2 RELATED WORK

Polarimetric BRDF models. Polarimetric BRDF (pBRDF) models take into account changes in the polarization state of light as it interacts with the corresponding surface. Several pBRDF models [Hyde IV et al. 2009; Jarabo and Arellano 2017; Mojzik et al. 2016; Priest and Gerner 2000] define reflection as a mixture of a rough polarizing specular lobe (by accounting for Fresnel interactions in a microfacet model) and a depolarizing diffuse lobe. However, other works have shown diffuse (view independent) polarization effects [Baek et al. 2020; Ellis 1996; Maxwell et al. 1973; Sun 2007], which can be explained by multiple subsurface scattering events (which depolarize light), followed by a Fresnel transmission from inside the object to the air, which partially polarizes light [Atkinson and Hancock 2006].

Recent pBRDF models consider this diffuse polarizing effect [Baek et al. 2018; Cui et al. 2017; Kadambi et al. 2015], and even leverage it to estimate surface normals. Our pBRDF model includes both polarizing diffuse and specular lobes, plus a new single scattering lobe, thus providing an accurate match against *measured* ground-truth data [Baek et al. 2020].

Polarimetric imaging. Polarization information has been used for a wide range of imaging purposes, such as dehazing [Liu et al. 2015], elimination of specular highlights [Yang et al. 2016], or new image editing techniques [del Molino and Muñoz 2019]. However, separating specular and diffuse polarization from reflected light is an open research problem due to the complex changes in polarization caused by surface scattering.

Some works take advantage of the polarizing effect of the specular component to estimate reflectance parameters and/or geometry. Ma et al. [2007] separate diffuse reflectance from specular components using polarized gradient illumination. More complete appearance models, including per-pixel diffuse and specular albedos, global roughness, and normal map have been proposed: Ghosh et al. [2008] extract layers of skin reflectance using polarization-difference images and data-driven techniques, for the particular case of faces. Other works leverage circularly polarized light [Ghosh et al. 2010], polarized gradient illumination [Ghosh et al. 2011], outdoors sky light [Riviere et al. 2017], or including cross-polarization filters in cameras [Riviere et al. 2020]. However, the high-frequency behavior and angular dependency of the specular reflection require multiple views and/or large-scale lighting setups to be able to find and leverage the specular component.

Another strategy considers the polarization effect of the diffuse reflection state as a function of the azimuth angle of the surface normal, given the Fresnel transmission from the object to the air. This has been used for geometry reconstruction (SfP, structure from polarization), estimating geometry and normals from single view polarimetric images [Atkinson and Hancock 2006; Huynh et al. 2013; Miyazaki et al. 2003; Tozza et al. 2017] or multiple views [Cui et al.

---

[1]https://github.com/KAIST-VCLAB/SparseEllipsometry.git

2017, 2019; Zhao et al. 2020; Zhu and Smith 2019]. Other methods have used deep neural networks to reconstruct both normals and spatially-varying material properties (i.e., SVBRDF) based on the same diffuse polarization cues [Ba et al. 2020; Deschaintre et al. 2021; Lei et al. 2021]. Since light depolarizes as it enters the object and given that the diffuse reflection is low frequency, these methods work even under unknown lighting conditions, while generally requiring simpler setups. However, the specular component of reflectance is not properly accounted for, which may lead to errors. Moreover, these existing methods leverage polarization information mainly to estimate diffuse albedo and normal maps, but they do not acquire complete polarimetric reflectance information, such as full Mueller matrices and indices of refraction.

Baek et al. [2018] introduced a pBRDF model as a linear combination of polarizing diffuse and specular components. Since then, there have been works on structure from polarization methods that account for both polarizing effects [Ding et al. 2021; Fukao et al. 2021]. However, these methods require a full Mueller matrix per pixel, which involves multiple shots changing the polarization state of the incident light. This requires rotation by hardware, which translates into heavy, sophisticated capture systems. These complex Mueller matrix measurements have also been used for separating components of light transport [Baek and Heide 2021] and for measuring pBRDFs [Baek et al. 2020]. Our work also considers the effect of both polarizing diffuse and specular components but, in contrast, it only requires a single Stokes vector per pixel. Consequently, it does not require a heavy polarimetric control of external light sources, leading to a compact hand-held capture device. In contrast, our portable design allows us to integrate per-pixel Stokes vectors observations from multiple views, enabling for the first time simultaneous acquisition of full polarimetric SVBRDF (including 3D Mueller matrix and index of refraction) and 3D shape.

3D geometry and SVBRDF acquisition. Traditionally, simultaneous acquisition of geometry and SVBRDF required large-scale specialized setups, such as light stages including polarized light sources, multiple cameras and/or projectors for structured lighting [Ghosh et al. 2010, 2008; Ma et al. 2007]. These setups have become progressively simpler, requiring a professional setup with multiple cameras and polarized lights [Ghosh et al. 2011], a rotating LED pattern for spherical harmonics [Tunwattanapong et al. 2013], controlled front LED lighting with multiple cameras [Gotardo et al. 2018], or spherical LED lighting with a single camera [Kampouris et al. 2018].

Other works focus on further simplifying the hardware setup for the capture, relying on photometric stereo [Zhou et al. 2013], calibrated environments [Oxholm and Nishino 2014], RGB-D information [Wu et al. 2016], video sequences [Xia et al. 2016], unstructured flash photographies [Nam et al. 2018], or pretrained structured LED illumination [Ma et al. 2021]. More recently, NeRF networks [Mildenhall et al. 2020] are able to reconstruct geometry and appearance parameters from images in arbitrary lighting condition [Boss et al. 2021; Srinivasan et al. 2021]. Our capture system also consists on a simple and hand-held setup that includes a flashlight, a polarizer, and polarization camera. Different from existing works, however, we not only acquire 3D geometry and SVBRDF, but also polarization.

3 POLARIMETRIC IMAGE FORMATION

3.1 Background on Polarization

The Stokes vector $\mathbf{s} = [s_0, s_1, s_2, s_3]^\top$ is a four-dimensional quantity that describes the polarization state of light. s_0 represents total radiance, while s_1, s_2, and s_3 are the polarized components defined by the degree of polarization ψ, polarization angle ξ, ellipticity angle ζ as $\mathbf{s} = [s_0, s_0\psi \cos 2\zeta \cos 2\xi, s_0\psi \cos 2\zeta \sin 2\xi, s_0\psi \sin 2\zeta]$. The s_1, s_2 and s_3 components describe horizontal, linearly diagonal, and circular polarization, respectively.

The Mueller matrix $\mathbf{M}$ represents a transformation of the polarization state of light represented by a Stokes vector: $\mathbf{s}_a = \mathbf{M}\mathbf{s}_b$, where $\mathbf{s}_{a,b}$ are the Stokes vectors before and after any transformation event, such as a change of coordinates, reflection, transmission or filtering.

A change on the polarization state after a reflection or transmission on an interface depends on Fresnel equations, which indicates that light polarized along the axis parallel to the plane of incidence is affected differently than light polarized perpendicular to that plane of incidence. Therefore, before the interaction, we need to align one of the axis (the y-axis in our case) to be parallel to the plane of incidence, which requires a rotation of the local frame (see Section 3.2). Specifically, the counterclockwise rotation with angle ϑ is represented by the following matrix $\mathbf{C}$ as

$$\mathbf{C}(\vartheta) = \begin{bmatrix} 1 & 0 & 0 & 0 \\ 0 & \cos 2\vartheta & \sin 2\vartheta & 0 \\ 0 & -\sin 2\vartheta & \cos 2\vartheta & 0 \\ 0 & 0 & 0 & 1 \end{bmatrix}. \tag{1}$$

Once in the adequate local frame, transmission and reflection of light can be represented by the Fresnel matrix $\mathbf{F}$:

$$\mathbf{F}^{F \in \{T,R\}} = \begin{bmatrix} \frac{F^\perp + F^\parallel}{2} & \frac{F^\perp - F^\parallel}{2} & 0 & 0 \\ \frac{F^\perp - F^\parallel}{2} & \frac{F^\perp + F^\parallel}{2} & 0 & 0 \\ 0 & 0 & \sqrt{F^\perp F^\parallel} \cos \delta & \sqrt{F^\perp F^\parallel} \sin \delta \\ 0 & 0 & -\sqrt{F^\perp F^\parallel} \sin \delta & \sqrt{F^\perp F^\parallel} \cos \delta \end{bmatrix}, \tag{2}$$

where $F \in \{T, R\}$ represents the Fresnel transmission (T) or reflection (R) coefficients, and δ is the retardation (delay) phase shift (0 when the incident angle is larger than the Brewster angle, π otherwise). $F^\perp$ and $F^\parallel$ are the Fresnel coefficients for the perpendicular and parallel components with respect to the plane of incidence (see the work of Wilkie and Weidlich [2012] for a complete description of polarized light). In the following F will refer to T or R, depending on the specific interaction (transmission or reflection) being considered. For convenience, notations are summarized in Table 2.

3.2 Polarimetric Reflectance Model

The light transport of polarized light can be defined in terms of the Stokes vector and the pBRDF as

$$\mathbf{s}_o = S\mathbf{P}(\omega_i, \omega_o)\mathbf{s}_i. \tag{3}$$

where $S = \frac{(\mathbf{n} \cdot \omega_i)}{d^2}$ is the shading term including light attenuation, d is the distance between the light and the surface and $\mathbf{P}(\omega_i, \omega_o)$ is the pBRDF that yields a Mueller matrix for a specific incoming and outgoing direction.
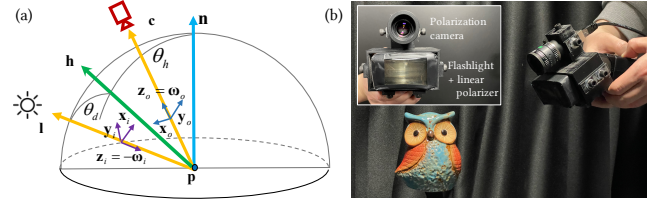
Fig. 2. (a) Our polarimetric coordinate system. (b) Our handheld polarimetric imaging setup consisting of a polarimetric camera and a photographic flashlight.
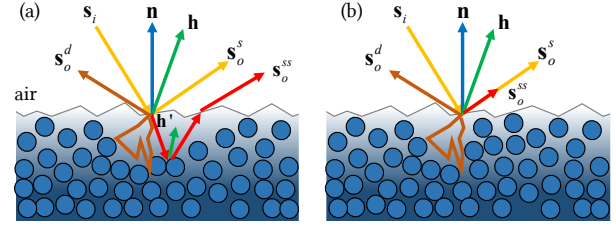

Fig. 3. (a) Geometry of our polarimetric scattering model. The $\mathbf{s}_o^s$ yellow vector represents the specular term, the brown vector $\mathbf{s}_o^d$ represents the diffuse term, and the red vector $\mathbf{s}_o^{ss}$ represents our additional single scattering term. (b) Our simplified scattering model for polarimetric inverse rendering.

Recent pBRDF models follow microfacet theory [Cook and Torrance 1982; Lee et al. 2018; Torrance and Sparrow 1967] and separate reflectance into diffuse and specular terms [Baek and Heide 2021; Baek et al. 2018]. However, our experiments have shown that the combination of those two lobes does not match captured datasets for polarimetric appearance [Baek et al. 2020]. We thus introduce a new additional term that takes into account *single scattering* effects; our resulting model provides a better fit against captured polarization data (see Section 6.2).

Our new polarimetric pBRDF model can then be expressed as

$$\mathbf{P} = \mathbf{P}^d + \mathbf{P}^s + \mathbf{P}^{ss}, \tag{4}$$

where $\mathbf{P}^d$, $\mathbf{P}^s$ and $\mathbf{P}^{ss}$ are the pBRDF lobes of diffuse reflection, specular reflection, and single scattering, respectively. The dependency on $\boldsymbol{\omega}_i$ and $\boldsymbol{\omega}_o$ has been omitted for the sake of brevity.

Local polarization frame. Our coordinate system is defined by a local frame with three orthonormal vectors, where the z-axis follows the propagation of light, the y-axis is aligned with the camera up vector for outgoing light, and with the orthogonal direction of the horizontal linear polarization filter on the light for incoming light, and the x-axis is perpendicular to both (see Figure 2a). This is different from previous work [Baek et al. 2018] in that we do not need to flip axes for incoming and outgoing light; instead, the frame is rotated so that its y-axis is aligned to the plane of incidence, thus matching the expected orientation for Fresnel interactions. The plane of incidence is defined by the surface normal $\mathbf{n}$ for the diffuse lobe and by the halfway vector $\mathbf{h}$ for the specular and single scattering lobes. We define the polarimetric azimuth angles for incident and exitant light corresponding to these two planes, respectively: $\phi_{\{i,o\}} = \tan^{-1}((\mathbf{n} \cdot \mathbf{y}_{\{i,o\}})/(\mathbf{n} \cdot \mathbf{x}_{\{i,o\}}))$ and $\varphi_{\{i,o\}} = \tan^{-1}((\mathbf{h} \cdot \mathbf{y}_{\{i,o\}})/(\mathbf{h} \cdot \mathbf{x}_{\{i,o\}}))$. Therefore, the corresponding rotation angles required to match the incident and exitant frames to the interaction plane are $\phi_{\{i,o\}}^{\llcorner} = \phi_{\{i,o\}} - \pi/2$ and $\varphi_{\{i,o\}}^{\llcorner} = \varphi_{\{i,o\}} - \pi/2$, respectively.

Diffuse and specular terms. We adopt the diffuse and specular terms from state-of-the-art pBRDF models [Baek and Heide 2021; Baek et al. 2018], which we briefly summarize here for completeness. *Polarized diffuse reflection* is formulated as

$$\mathbf{P}^d = \mathbf{C}_{n \to o}\left(-\phi_o^{\llcorner}\right) \mathbf{F}^T\left(\theta_o; \eta\right) \mathbf{D}\left(\rho_d\right) \mathbf{F}^T\left(\theta_i; \eta\right) \mathbf{C}_{i \to n}\left(\phi_i^{\llcorner}\right), \tag{5}$$

where $\mathbf{D}$ is the depolarization matrix with diffuse albedo ρ_d. In Mueller matrix form, $\mathbf{P}^d$ is

$$\mathbf{P}^d = \rho_d \begin{bmatrix} T_o^+ T_i^+ & -T_o^+ T_i^- \beta_i & -T_o^+ T_i^- \alpha_i & 0 \\ -T_o^- T_i^+ \beta_o & T_o^- T_i^- \beta_i \beta_o & T_o^- T_i^- \alpha_i \beta_o & 0 \\ -T_o^- T_i^+ \alpha_o & T_o^- T_i^- \alpha_o \beta_i & T_o^- T_i^- \alpha_o \alpha_i & 0 \\ 0 & 0 & 0 & 0 \end{bmatrix}, \tag{6}$$

where $\alpha_{\{i,o\}}$ and $\beta_{\{i,o\}}$ indicate $\sin(2\phi_{\{i,o\}})$ and $\cos(2\phi_{\{i,o\}})$, respectively. Here $T_{\{i,o\}}^+$ and $T_{\{i,o\}}^-$ are computed from incident/exitant Fresnel transmission coefficients, $(T_{\{i,o\}}^{\perp} + T_{\{i,o\}}^{\|})/2$ and $(T_{\{i,o\}}^{\perp} - T_{\{i,o\}}^{\|})/2$.

Polarized specular reflection, on the other hand, is described as a single-bounce reflection on the microfacets as

$$\mathbf{P}^s = \kappa_s \mathbf{C}_{h \to o}\left(-\varphi_o^{\llcorner}\right) \mathbf{F}^R\left(\theta_d; \eta\right) \mathbf{C}_{i \to h}\left(\varphi_i^{\llcorner}\right), \tag{7}$$

where $\kappa_s = \rho_s \frac{D(\theta_h; \sigma_s) G(\theta_i, \theta_o; \sigma_s)}{4(\mathbf{n} \cdot \boldsymbol{\omega}_i)(\mathbf{n} \cdot \boldsymbol{\omega}_o)}$ is the specular reflection term, D is the normal GGX distribution function [Walter et al. 2007], σ_s is surface roughness, G is Smith's geometric attenuation function of shadowing/masking [Heitz 2014], and ρ_s is the specular albedo. Assuming that our target surface is dielectric, specular reflection can be considered monochromatic. The specular lobe $\mathbf{P}^s$ can be expressed in Mueller matrix form as

$$\mathbf{P}^s = \tag{8}$$

$$\kappa_s \begin{bmatrix} R^+ & -R^- \gamma_i & -R^- \chi_i & 0 \\ -R^- \gamma_o & R^+ \gamma_i \gamma_o + R^\times \chi_i \chi_o \cos\delta & R^+ \chi_i \gamma_o - R^\times \gamma_i \chi_o \cos\delta & R^\times \chi_o \sin\delta \\ -R^- \chi_o & R^+ \gamma_i \chi_o - R^\times \chi_i \gamma_o \cos\delta & R^+ \chi_i \chi_o + R^\times \gamma_i \gamma_o \cos\delta & -R^\times \gamma_o \sin\delta \\ 0 & -R^\times \chi_i \sin\delta & R^\times \gamma_i \sin\delta & R^\times \cos\delta \end{bmatrix},$$

where $\chi_{\{i,o\}}$ and $\gamma_{\{i,o\}}$ denote $\sin(2\varphi_{\{i,o\}})$ and $\cos(2\varphi_{\{i,o\}})$, respectively. For a dielectric surface $\cos\delta = -1$ when the incident angle is less than the Brewster angle, and 1 otherwise.

Single scattering term. We extend existing pBRDF models by incorporating a new *polarimetric single scattering* term, which yields a better match with captured data. In our model, the path of light for a single scattering event includes a Fresnel transmission into the object, a scattering reflection, and a second Fresnel transmission back into the air ($\mathbf{s}_o^{ss}$, see red vectors in Figure 3a). Different from specular reflection, color can change according to the albedo of the medium ρ_{ss}, while its angular distribution is a combination of the roughness of the surface (which affects Fresnel transmission) and the phase function $p(\boldsymbol{\omega}_i, \boldsymbol{\omega}_o)$. Our single-scattering term can thus

be modeled as

$$\mathbf{P}^{ss} = \mathbf{C}_{n \to o} \left(-\phi_o^{\llcorner}\right) \mathbf{F}^T \left(\theta_o; \eta\right) \mathbf{C}_{h' \to n} \left(-\varphi_o^{\llcorner'}\right) \mathbf{F}^R \left(\theta'_d; \eta_p\right) \quad (9)$$
$$\cdot \, r_{ss} \mathbf{C}_{n \to h'} \left(\varphi_i^{\llcorner'}\right) \mathbf{F}^T \left(\theta_i; \eta\right) \mathbf{C}_{i \to n} \left(\phi_i^{\llcorner}\right),$$

where $\varphi_{\{i,o\}}^{\llcorner'}$ is the rotation angle w.r.t. the medium's microfacet $\mathbf{h}'$ vector for incoming/outgoing rays (Figure 3a), and η and η_p are the indices of refraction for the surface and the single scattering interactions, respectively. The parameter r_{ss} represents the single-scattering BRDF [Hanrahan and Krueger 1993] as:

$$r_{ss} = \rho_{ss} p \left(\omega'_i, \omega'_o\right) \frac{1}{\mathbf{h}' \cdot \omega'_i + \mathbf{h}' \cdot \omega'_o}, \quad (10)$$

where directions ω'_i and ω'_o are deterministically calculated using Snell's Law, and the phase function $p \left(\omega'_i, \omega'_o\right)$ is the angular distribution that may be represented by Henyey-Greenstein's model [Henyey and Greenstein 1941].

While physically accurate, the model defined in Equation (9) is ill-posed and not suitable for inverse rendering, since the single scattering event is occluded from direct view after a refractive event with an unknown index of refraction. We therefore introduce a simplified model, approximating the physically-based behavior of our single scattering component and making it practical for imaging and inverse rendering applications. We make the following observations:

- Single scattering presents a polarization state similar to the polarization state of specular reflections [Ghosh et al. 2008].
- The angular distribution (roughness) of single scattering comes from the combination of the roughness of both Fresnel transmissions and the phase function.
- While specular reflection does not change color, single scattering modifies color according to the albedo and extinction of the medium.

From these observations, our single scattering component can be represented as an extension of the specular reflection term, with independent roughness and albedo parameters:

$$\mathbf{P}^{ss} = \kappa_{ss} \mathbf{C}_{h \to o} \left(-\varphi_o^{\llcorner}\right) \mathbf{F}^R \left(\theta_d; \eta\right) \mathbf{C}_{i \to h} \left(\varphi_i^{\llcorner}\right), \quad (11)$$

where $\kappa_{ss} = \rho_{ss} \frac{D(\theta_h; \sigma_{ss}) G(\theta_i, \theta_o; \sigma_{ss})}{4(\mathbf{n} \cdot \omega_i)(\mathbf{n} \cdot \omega_o)}$ describes the single scattering lobe, and σ_{ss} represents surface roughness for single scattering. Note that the single scattering albedo ρ_{ss} is a colored vector, as opposed to the single-value specular component.

Mueller matrix representation for the single scattering lobe is

$$\mathbf{P}^{ss} = \quad (12)$$

$$\kappa_{ss} \begin{bmatrix} R^+ & -R^- \gamma_i & -R^- \chi_i & 0 \\ -R^- \gamma_o & R^+ \gamma_i \gamma_o + R^\times \chi_i \chi_o \cos\delta & R^+ \chi_i \gamma_o - R^\times \gamma_i \chi_o \cos\delta & R^\times \chi_o \sin\delta \\ -R^- \chi_o & R^+ \gamma_i \chi_o - R^\times \chi_i \gamma_o \cos\delta & R^+ \chi_i \chi_o + R^\times \gamma_i \gamma_o \cos\delta & -R^\times \gamma_o \sin\delta \\ 0 & -R^\times \chi_i \sin\delta & R^\times \gamma_i \sin\delta & R^\times \cos\delta \end{bmatrix},$$

where $\chi_{\{i,o\}}$, $\gamma_{\{i,o\}}$ and $\cos\delta$ are the same as in specular reflection.

3.3 Portable Acquisition Setup

Capturing full polarimetric appearance information of an object requires exhaustive sampling in both traditional ellipsometry [Azzam 1978] and image-based ellipsometry [Baek et al. 2020] methods, which usually takes between two and five days. In addition, the process needs a complex tabletop setup, with multiple rotating

polarization filters and retarders. We aim for a more usable, efficient and practical approach, for which we leverage our (spatially varying) pBRDF model (Section 3.2); while simpler and easier to approximate, it provides a very good match with full polarimetric measured data [Baek et al. 2020], as our results will show.

We propose a simple setup that consists of a polarimetric camera with *fixed* linear polarization filters at four different orientations (0°, 45°, 90°, and 135°), and a photographic flashlight with a fixed linear polarization filter at 0° angle. As shown in Figure 2(b), the light and the camera are mounted close together in a near-coaxial setup (around 3.5°, but it needs to be calibrated), leading to a small enough device for handheld acquisition. Our input is a set of multiple RAW images including four different polarization angles. The intensity of the flash varies randomly for each captured image (between {1/4, 1/8, 1/16} of its maximum intensity), so per-vertex HDR radiance can be recovered [Debevec and Malik 1997].

Instead of rotating optical components in a complex, fixed tabletop setup, we leverage the portable form factor of our capture device and develop a *single-view* image formation model (Section 3.4), and apply this model in the optimization of multiple unstructured observations (Section 4).

3.4 Image Formation Model

Section 3.2 introduces our complete pBRDF model. We now customize such a model to formulate light transport specifically for our acquisition system where the camera and flashlight are narrowly placed and oriented (see Section 3.3), and represent the physical magnitudes of our pBRDF model as observations over the four captured images.

This narrow setup has been used in a recent study [Baek et al. 2018]. It is clearly beneficial in polarimetric imaging because it enables many simplifications of polarized interactions with surfaces. Our hardware design takes the advantage of this simplification by inheriting this near-coaxial setup. However, the approach by Baek et al. [2018] is based on ellipsometry, exhaustively capturing sixteen combinations of incident/exitant polarization states as input, while our approach only requires four combinations (the four linear filters of the camera and only one for the light source).

Some of these simplifications are purely geometrical: as light and camera rays are only separated by approximately 3.5°, we can assume $\omega_i \approx \omega_o$ and, as the optical elements are equally oriented, incident and exitant local polarization frames are also related as $\phi_i \approx \pi - \phi_o$ and $\varphi_i \approx 2\pi - \varphi_o$ so therefore $\alpha_i \approx -\alpha_o$, $\beta_i \approx \beta_o$, $\chi_i \approx -\chi_o$ and $\gamma_i \approx \gamma_o$. Furthermore, incident angle is by definition below Brewster angle so $\cos\delta = -1$ for both specular and single scattering terms. The geometrical relations defined by this narrow geometry are illustrated in Figure 4.

Last, the parallel and perpendicular components of the Fresnel reflection become close to each other ($R^\parallel \approx R^\perp$), so that $R^- \approx 0$ and $R^+ \approx R^\times$ and light from the diffuse interaction gets depolarized through multiple subsurface scattering so the degree of polarization of incoming light $T_o^- T_i^- \approx 0$.

Adding the three lobes defined in Equations (6), (8), and (12), and taking into account these simplifications, our full pBRDF as a
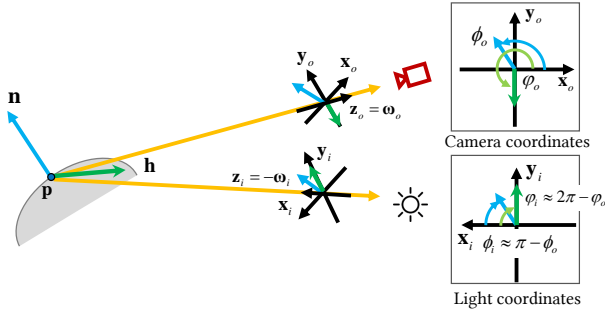
Fig. 4. The geometry of our portable setup is narrow, with the flashlight slightly below the camera sensor. This establishes several geometrical relationships between the light polarization frame, the camera polarization frame, surface normal n, and halfway vector h. This affects the relationship between the polarimetric azimuths for the diffuse lobe ($\phi_i \approx \pi - \phi_o$) with respect to the normal. Also, the projection of the halfway vector into the incident polarization plane points towards the exitant frame and vice versa, therefore establishing a relation between the corresponding polarization azimuths ($\varphi_i \approx 2\pi - \varphi_o$).

Mueller matrix can be obtained as

$$\mathbf{P} \approx \begin{bmatrix} \rho_d T^+ T^+ + \kappa_s R^+ + \kappa_{ss} R^+ & -\rho_d T^- T^+ \beta & \rho_d T^- T^+ \alpha & 0 \\ -\rho_d T^- T^+ \beta & \kappa_s R^+ + \kappa_{ss} R^+ & 0 & 0 \\ -\rho_d T^- T^+ \alpha & 0 & -\kappa_s R^+ - \kappa_{ss} R^+ & 0 \\ 0 & 0 & 0 & -\kappa_s R^+ - \kappa_{ss} R^+ \end{bmatrix}.$$
(13)

Since the light source has a linear polarizer at $0°$, the incident light is linearly polarized so its Stokes vector is $\mathbf{s}_i = [1, 1, 0, 0]^\top$. Plugging this into Equation (3) leads to the reflected Stokes vector $\mathbf{s}_o$ as

$$\mathbf{s}_o = S\mathbf{P}\mathbf{s}_i = S \begin{bmatrix} \rho_d T^+ T^+ - \rho_d T^- T^+ \beta + \kappa_s R^+ + \kappa_{ss} R^+ \\ -\rho_d T^- T^+ \beta + \kappa_s R^+ + \kappa_{ss} R^+ \\ -\rho_d T^- T^+ \alpha \\ 0 \end{bmatrix}.$$
(14)

Given the fixed polarization filters, our camera captures a four-channel color image including four different polarization orientations. The Stokes image $\mathbf{I}$ can then be expressed as

$$\mathbf{I} = \begin{bmatrix} I_0 \\ I_{90} \\ I_{45} \\ I_{135} \end{bmatrix} = \begin{bmatrix} 1 & 1 & 0 & 0 \\ 1 & -1 & 0 & 0 \\ 1 & 0 & 1 & 0 \\ 1 & 0 & -1 & 0 \end{bmatrix} \mathbf{s}_o$$

$$= \frac{S}{2} \begin{bmatrix} \rho_d T^+ T^+ - 2\rho_d T^+ T^- \beta + 2\kappa_s R^+ + 2\kappa_{ss} R^+ \\ \rho_d T^+ T^+ \\ \rho_d T^+ T^+ - \rho_d T^+ T^- \beta + \kappa_s R^+ + \kappa_{ss} R^+ - \rho_d T^- T^+ \alpha \\ \rho_d T^+ T^+ - \rho_d T^+ T^- \beta + \kappa_s R^+ + \kappa_{ss} R^+ + \rho_d T^- T^+ \alpha \end{bmatrix}.$$
(15)

While previous work required a dense set of angular samples [Baek et al. 2018], the four components of $\mathbf{I}$ provide valuable enough information about the pBRDF. First, I_{90} refers to the diffuse lobe, so we define our first *diffuse shading* observation I^d as

$$I^d = S\rho_d T^+ T^+ = 2I_{90}.$$
(16)

Information about the diffuse term can also be obtained from the subtraction of I_{45} and I_{135}, which we define as a *diffuse polarization* observation I^α as

$$I^\alpha = S\rho_d T^- T^+ \alpha = I_{135} - I_{45}.$$
(17)

Fig. 5. Overview of our method. Iteratively, we alternate joint estimations of polarimetric SVBRDF $\mathbf{P}$ and shading normals $\mathbf{N}$ with reconstructions of 3D geometry $\mathbf{X}$.

Last, by substituting I_{90} in I_0, we can obtain a combination of specular reflection, single scattering and oriented diffuse parameters. We define this combination as the *specular-dominant polarization* observation I^s as

$$I^s = S \left(\kappa_s R^+ + \kappa_{ss} R^+ - \rho_d T^- T^+ \beta \right) = I_0 - I_{90}.$$
(18)

In the following section, we show how to leverage these single-image observations to optimize spatially-varying pBRDF parameters and surface geometry from *multiple* views.

4 MULTIVIEW RECONSTRUCTION OF POLARIMETRIC SVBRDF AND SHAPE

4.1 Overview

An overview of our method can be seen in Figure 5. Our input consists of a set of K unstructured polarimetric photographs $\mathbf{I} = \{I_k\}$ taken with our portable hardware (Section 3.3) and interpreted through our image formation model (Section 3.4). First, an initialization step linearizes I_k and obtains camera parameters and a rough base geometry using conventional 3D reconstruction techniques (Section 4.2). We then iteratively reconstruct polarimetric SVBRDF information $\mathbf{P}$ and shading normals $\mathbf{N}$ through inverse rendering (Section 4.3), and then reconstruct detailed 3D geometry $\mathbf{X}$ by means of Poisson surface reconstruction (Section 4.4). In the last step, we update the polarimetric SVBRDF $\mathbf{P}$ from the final 3D geometry.

4.2 Initialization

From our cross-polarized diffuse observations in the captured data, defined as I^d in Equation (16), we first obtain a dense 3D point cloud with normal information and camera poses, which will provide the correspondences between 3D points and pixels in multiple views, using Structure-from-Motion (SfM) [Schönberger et al. 2016]. To mitigate the inherent reconstruction errors from SfM, we first create a low-resolution mesh (2^7-level octree in the voxel grid) using the screened Poisson surface reconstruction [Kazhdan and Hoppe 2013], then subdivide it to obtain a finer mesh (2^9-level). This finer mesh is used as the initial geometry of our iterative technique, and might still miss geometric details due to the limitations of SfM. The geometry stage of our iterative algorithm (Section 4.4) recovers these details.

4.3 Optimizing Polarimetric SVBRDF and Normals

We jointly optimize polarimetric SVBRDF and normals by minimizing the sum of four loss terms as

$$\min_{\eta, \sigma_s, \rho_s, \rho_{ss}, \rho_d, \mathbf{n}} \left(\lambda_1 \mathcal{L}_\psi + \lambda_2 \mathcal{L}_d + \lambda_3 \mathcal{L}_s + \lambda_4 \mathcal{L}_\phi \right),$$
(19)

where $\mathcal{L}_\psi$ is the refractive index loss, $\mathcal{L}_d$ is the diffuse loss, $\mathcal{L}_s$ is the specular and single scattering loss, and $\mathcal{L}_\phi$ is the normal loss. We set the weights to $\lambda_{\{1,3\}} = 1$, $\lambda_{\{2,4\}} = 100$. For efficiency, $\mathcal{L}_d$ and $\mathcal{L}_s$ are calculated by linear optimization, while $\mathcal{L}_\psi$ and $\mathcal{L}_\phi$ are

computed by nonlinear optimization, using the sequential quadratic programming method.

Refractive index loss $\mathcal{L}_\psi$. Existing approaches [Baek and Heide 2021; Baek et al. 2018] require dense angular samples, which force fixed acquisition setups. Our novel refractive index loss overcomes such angular density requirements, providing a more flexible capture setup. The key insight is that the degree of polarization (DoP) of the diffuse reflection depends on the refractive index and normal orientation can be represented as a ratio of Fresnel transmission functions ($\psi = |T^-/T^+|$). We thus define $\mathcal{L}_\psi$ as a loss function over DoP as

$$\mathcal{L}_\psi = \sum\nolimits_{k=1}^{K} w_k^v \left(\hat{\psi}\left(\eta, \theta_{o,k}\right) - \psi_k\right)^2, \qquad (20)$$

where $\hat{\psi}$ is the predicted DoP value for the k-th view, represented as $|T^-/T^+|$. Fresnel transmissions depend on normal orientation $\theta_{o,k}$ and index of refraction η (both being optimized with this loss function). The visibility weight w_k^v for this view is calculated as $w_k^v = v_k / \sum_{i=1}^{K} v_i$, where $v = \{0, 1\}$.

Our input does not provide a direct observed DoP value ψ_k, so we approximate it from our observations I^d, I^α, and I^s (Equations (16), (17), and (18) in Section 3.4). Our diffuse Mueller matrix, described in Equation (6), depends on two parameters: $\alpha = \sin(2\phi)$, and $\beta = \cos(2\phi)$. This leads to two diffusely polarized images $I^\alpha = -S\rho_d T^- T^+ \alpha$ and $I^\beta = -S\rho_d T^- T^+ \beta$, from which diffuse polarization can be obtained as $\Gamma = \sqrt{(I^\alpha)^2 + (I^\beta)^2}$, and ψ_k becomes

$$\psi = \left|\frac{\Gamma}{I^d}\right| = \left|\frac{S\rho_d T^+ T^-}{S\rho_d T^+ T^+}\right|, \qquad (21)$$

where Γ and I^d have their three color channels averaged into a single value. For simplicity, note that we have removed the subindex k referring to each individual view.

Different from I^α and I^d, I^β cannot be directly obtained from our input images. Instead, we obtain I^β by subtracting the polarimetric specular components $\kappa_s SR^+$ and $\kappa_{ss} SR^+$ from our specular-dominant polarization observation I^s, as

$$I^\beta = I^s - \kappa_s SR^+ - \kappa_{ss} SR^+, \qquad (22)$$

where the parameters' values come from the previous iteration. For the first iteration, we approximate $I^\beta \approx I^s$.

Diffuse Loss $\mathcal{L}_d$. We formulate our diffuse loss $\mathcal{L}_d$ by comparing the predicted diffuse image $\hat{I}_k^d$ with the captured image I_k^d for the k-th view as

$$\mathcal{L}_d = \sum\nolimits_{k=1}^{K} w_k^v \left(\hat{I}_k^d - I_k^d\right)^2, \qquad (23)$$

where the Fresnel transmission in $\hat{I}_k^d$, shown in Equation (16), is computed from the refractive index of the previous iteration (initially set to $\eta = 1.5$). Losses of each color channel are summed together.

Specular and single scattering loss $\mathcal{L}_s$. Despite using multiple photographs as input, the number of samples is often insufficient to estimate *per-vertex* specular and single scattering parameters, especially for very narrow specular lobes. To solve this, the approach by existing reconstruction methods [Alldrin et al. 2008; Baek et al. 2018; Chen et al. 2014; Lawrence et al. 2006; Nam et al. 2018, 2016; Wu and Zhou 2015; Zhou et al. 2016] is to obtain the specular parameters

of vertices with no suitable view by clustering vertices and assigning them the same specular parameters, which is prone to appearance parameter estimation errors due to imperfectness in the clustering algorithm. We instead apply a novel *specular augmentation* strategy to increment the number of per-vertex observations, by generating virtual samples from the specular and single scattering parameters of its local neighborhood.

Then, our specular and single scattering loss term is composed of two parts. The first, as expected, is the difference between the predicted specular and single scattering polarization $\hat{I}_k^s$ and the captured I_k^s for the k-th view, and the second is the difference between the predicted specular and single scattering $\hat{I}_m^s$ and the sample $\tilde{I}_m^s$ for a *virtual* m-th observation, as

$$\mathcal{L}_s = \sum\nolimits_{k=1}^{K} w_k^v \left(\hat{I}_k^s - I_k^s\right)^2 + \lambda_g \sum\nolimits_{m=1}^{M} w_m^a \left(\hat{I}_m^s - \tilde{I}_m^s\right)^2, \qquad (24)$$

where w^a is a normalized $\cos(\theta_h)$ weight, $m \in [1, ..., M]$ is the virtual observation index (we set M to 180 to cover $90°$), λ_g is the specular augmentation loss weight, set to 0.1 so that the loss function prioritices the match from real views over the virtual observations. Losses for each color channel are summed together.

To generate these new virtual views $\tilde{I}_m^s$, we assume that many similar vertices share similar material features, and thus vertices that share similar refractive index and diffuse albedo are more likely to share also specular and single scattering properties. We therefore define a four-dimensional feature vector that includes the refractive index and all three channels of the diffuse albedo, and use K-means to cluster vertices according to such features.

We then regress the specular and single scattering model parameters for each cluster by minimizing

$$\min_{\eta, \sigma_s, \sigma_{ss}, \rho_s, \rho_{ss}, \Delta\theta_h} \left(\mathcal{L}_\psi + \mathcal{L}_s' + \mathcal{L}_\theta\right), \qquad (25)$$

where $\mathcal{L}_s'$ represents the first loss term only in Equation (24), $\Delta\theta_h$ is a variable that accounts for potential θ_h errors in the measured samples (to which specular parameters are specially sensitive), and $\mathcal{L}_\theta = (\Delta\theta_h)^2$ is a regularization loss for $\Delta\theta_h$. This yields specular parameters per cluster. In contrast to previous works [Baek et al. 2018; Nam et al. 2018], the optimized specular parameters are not directly set for the vertices (which is very prone to errors over edges and high-frequency textures) but used to generate novel views to include in the loss function. We render these new views as per-vertex $\tilde{I}^s$ observations distributed uniformly in θ_h from zero to $90°$ at $0.5°$ intervals and include them into the loss function as defined in Equation (24).

Last, the calculation of the loss function for the real views requires the evaluation of the specular-dominant observations I^s as in Equation (18). I^s includes a term $-\rho_d ST^- T^+ \beta$ which is noisy, relatively weak and cancels out at different views, so we approximate it to zero. We assume dielectric surfaces, and thus we use a single channel for specular albedo and three channels for the single scattering albedo.

Normal loss $\mathcal{L}_\phi$. The zenith angle θ_o of the normal is already accounted for by the aforementioned loss terms for the index of refractive, diffuse, and specular polarization, since it affects the Fresnel terms. Therefore, our normal loss term deals only with the azimuth angle ϕ_o. However, ϕ_o contains an ambiguity of π radians,

which leads to errors in the reconstructions; this is known as the azimuthal ambiguity [Atkinson and Hancock 2006; Kadambi et al. 2015]. In our work, we minimize the errors caused by this ambiguity leveraging our multiple observations from different view angles. Our normal loss is formulated as

$$\mathcal{L}_\phi = \sum_{k=1}^{K} 2w_k^p \left(1 - \cos \left(2\hat{\phi}_{o,k} - 2\phi_{I,k} \right) \right), \qquad (26)$$

where $\hat{\phi}_{o,k}$ is the azimuth angle of the estimated normal at the k-th view and $\phi_{I,k}$ is the observed azimuth angle from diffuse polarization computed by $2\phi_{I,k} = \tan^{-1}(I_k^\alpha / I_k^\beta)$. The diffuse polarization weight $w_k^p = w_k^v \Gamma_k^2$ prioritizes stronger diffuse polarization signals.

4.4 Optimizing Geometry

After estimating the polarimetric SVBRDF **P** and shading normals **N**, we then reconstruct the geometry **X** so that it agrees with the polarimetric observations. We update this geometry with estimated shading normals, following a recent work [Nam et al. 2018]. Since the shading normals **N** may contain high-frequency noise, we choose the screened Poisson method [Kazhdan and Hoppe 2013], designed to reconstruct implicit surfaces in a voxel grid in a coarse-to-fine approach. This leads to a robust performance when integrating noisy surface normals into 3D geometry.

In the last iteration, after the denoised final shading normals **N** are obtained from the final geometry **X**, we only optimize the polarimetric SVBRDF **P** one last time.

5 IMPLEMENTATION DETAILS

Experimental setup. We build our capture setup from two off-the-shelf components: a polarization machine vision camera (LUCID PHX050S-QC), and a flashlight (Nikon Speedlight SB24) covered with a linear polarization film. The two components are supported together with a custom 3D-printed structure (see Figures 1 and 2b). To properly capture HDR specular reflections we rely on multi-bracketing [Debevec and Malik 1997], using three flash levels at $\{1/4, 1/8, 1/16\}$ of its maximum intensity per view. We capture around 100 and 300 views per object. The exact number of views for each of our results can be found in the supplemental material.

Calibration. To estimate the exact geometric relation between the camera and the flash (since they cannot be perfectly coaxial), we use the mirror reflections of the flashlight on multiple stainless spheres with a known radius. We place them on a grid at regular 25mm intervals, and estimate the light position with respect to the camera by accounting for the trigonometry of the specular reflections, following Lensch et al. [2003]. In our device, the separation between the camera and the light source is 5 cm, so the angle between light and camera rays is ~3.5° when the captured object is at a distance of around 80–100 cm. The intrinsic geometry of the polarization camera is calibrated using the method by Zhang [2000]. Last, we also calibrate color reproduction by estimating a linear matrix from RAW RGB channels to the sRGB color channels using a Macbeth ColorChecker. Note that these calibrations only need to be performed once per device.

Optimization. The size of our reconstructed models varies between $500,000$ and $800,000$ vertices, with pBRDF parameters stored as per-vertex attributes. We optimize Equation (19) by means of a nonlinear optimizer, sequential quadratic programming (SQP), using fmincon in MATLAB. One iteration takes about one hour in a desktop computer with an Intel i9-12900 CPU 3.2 GHz and 64 GB of memory and an NVIDIA Titan RTX GPU (similar to previous approaches). Final results are produced after ten iterations.

6 VALIDATION

6.1 pBRDFs Models

First, we evaluate the accuracy of our proposed physically-based and practical pBRDF models against actual pBRDF measurements by Baek et al. [2020], both at 111° near the Brewster angle of the object, and at 9°, closest to our coaxial setup. Figure 6 shows the resulting Mueller matrices, along with false-color difference maps. Despite its simplifications, our practical model offers accurate results while being suitable for optimization.

6.2 Single Scattering

Our new single scattering component, as defined by Equation (11), is different from the specular component in two ways: first, it presents a *colored* albedo which is different from the diffuse component, while the specular reflection retains the color of the illumination. Second, it has an independent roughness parameter, which approximates two Fresnel transmissions and a single subsurface interaction with an unknown phase function. The combination of colored albedo and independent roughness leads to clearly different single scattering and specular components in most scenes. Figure 7 shows side-by-side comparisons between captured polarimetric data from a red billiard ball [Baek et al. 2020] and the results optimizing our practical pBRDF model (Section 3.4). We use the measurements closest to the coaxial angle (9° between the light and the sensor in [Baek et al. 2020], compared to 3.5° in our setup). This shows a good agreement with measured data.

6.3 Index of Refraction

The index of refraction is the most unstable parameter when optimizing our model, since it affects all the lobes of the polarimetric SVBRDF in different ways, with ambiguities regarding how its variation affects appearance. We validate the accuracy of our optimized index of refraction against real-world materials from the existing pBRDF dataset of Baek et al. [2020]. As input, we use synthetic views generated from the captured dataset. The ground truth index of refraction from measured data is obtained from the Brewster angle as explained in the comprehensive work of Collett [2005].

Table 1 shows the results. Despite needing only four linear polarization measurements per view instead of the dense measurements of full ellipsometry, the accuracy of our method is consistently high.

6.4 Impact of Specular Augmentation

Next, we evaluate the impact of our specular augmentation algorithm (Section 4.3). Figure 8(a) shows one of our input photographs; for this particular view, there are almost no specular reflections in the vertex indicated by the arrow. Figure 8(b) shows a scatter plot of the captured specular-dominant samples I^s, where each black dot indicates a specular observation projected onto the normal space
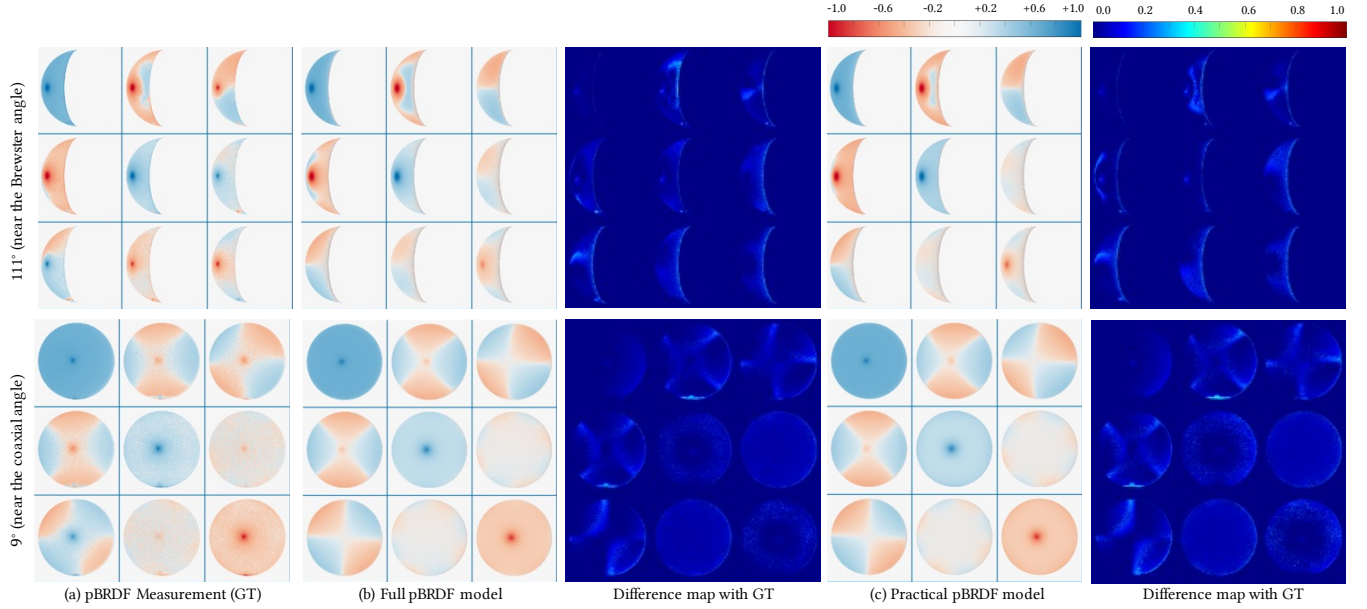
Fig. 6. Validation of our pBRDF models by comparing the resulting Mueller matrices, at two different angles. (a) Ground-truth, captured data of an organic thermoplastic polymer object (PEEK) [Baek et al. 2020]. (b) Our full pBRDF model and its difference map with respect to the ground truth. (c) Our practical model and its difference map. Despite the simplifications introduced in our practical model, it offers accurate results while being suitable for optimization.
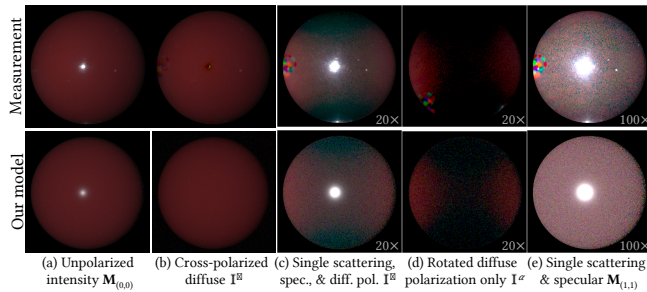

Fig. 7. Top: measured polarimetric data from a red billiard ball [Baek et al. 2020] (the rainbow speckles are caused by lens flare effects in the capture system). Bottom: results from our model. Columns (c), (d), and (e) have been amplified by the indicated factors for visualization purposes.
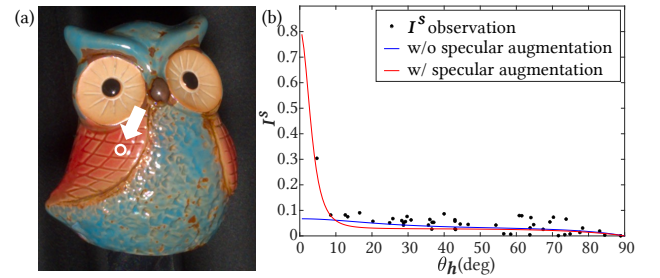

Fig. 8. The sparse nature of our input images would lead to wrong estimations of specular reflections. (a) Example input image without specular information in the highlighted area. (b) The resulting specular reflection functions with and without data augmentation (red and blue lines, respectively).

Table 1. Comparison between the ground truth index of refraction of several objects measured by Baek et al. [2020] and our optimized results.

Material	η_m	η_{ours}	error
White billiard	1.463	1.465	0.10%
Red billiard	1.485	1.476	0.61%
Green billiard	1.503	1.476	1.80%
POM	1.462	1.457	0.34%
Fake pearl	2.295	2.244	2.22%
Yellow silicone	1.303	1.337	2.61%
PEEK	1.663	1.617	2.77%
Average			1.49%

of the vertex in the 3D object. The blue line shows the profile of the resulting regressed specular reflection, which would translate into an overly diffuse appearance. The red line represents the optimized profile after our specular data augmentation method, which

recovers the missing specular information and better fits the sparse captured data. For this owl scene, we obtain a PSNR of 34.0 dB with our proposed data augmentation, which drops to 30.8 dB without it.

7 RESULTS

7.1 Comparisons with Other Methods

We first compare our shape and appearance reconstructions against two recent state-of-the-art methods. Nam et al. [2018] reconstruct 3D models with conventional SVBRDF from multiview stereo as input, while Baek et al. [2018] estimate polarimetric SVBRDF and surface normals from a given geometry in a single view. Figure 9 shows the results when generating novel views under different illumination. Nam's method estimates the normal distribution function

Photograph and scanned geometry   Nam et al. 2018   Baek et al. 2018   Ours
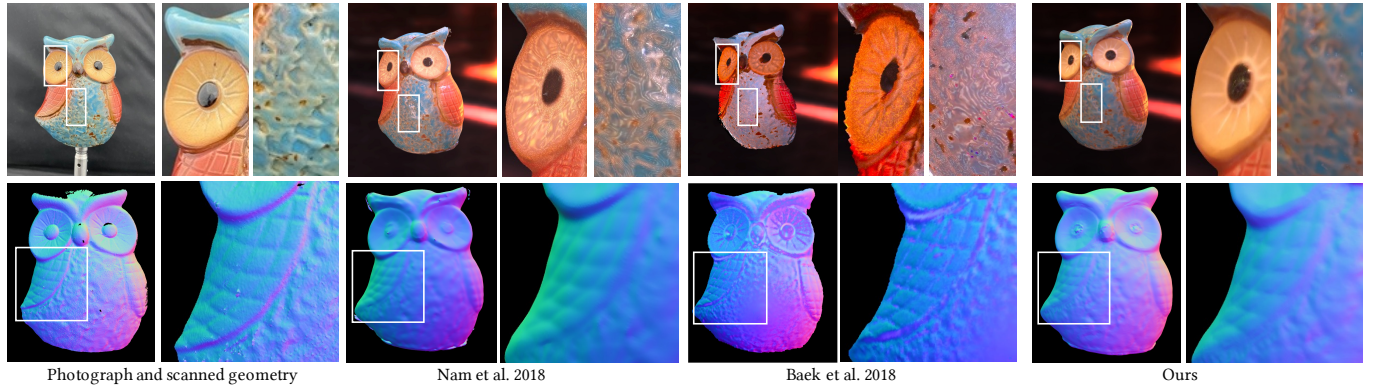
Fig. 9. Comparison of our method with two state-of-the-art techniques: a multiview 3D reconstruction method [Nam et al. 2018], and a polarimetric reconstruction method [Baek et al. 2018]. The former yields visible overfitting errors in the reflectance, with overly smooth geometric details (see also Figure 10). The latter suffers from overfitting and clustering artifacts in reflectance, as well as geometric distortions in novel views.

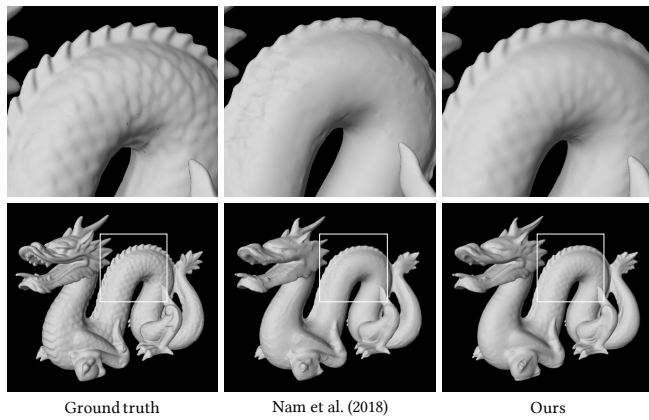Ground truth   Nam et al. (2018)   Ours

Fig. 10. Accuracy of our 3D reconstructions against a state-of-the-art multiview reconstruction method [Nam et al. 2018]. Leveraging information about the polarization of light allows us to recover more geometrical details.

as a tabulated function, which is convenient for representing specular reflection but it often causes visible artifacts in the recovered reflectance, due to overfitting during optimization. This is clearly visible in the eye region and, to a lesser extent, in the swirling patterns on the body. Baek's method, on the other hand, also suffers from overfitting artifacts in the reflectance, while showing additional clustering artifacts as well. Moreover, being a single-view method, it cannot reconstruct the full 3D geometry, which leads to visible distortions when rendering novel views. In contrast, our method does not suffer from overfitting nor clustering artifacts in the reflectance, while our geometric reconstruction is more detailed, and closer to the ground truth from a commercial 3D laser scanner (NextEngine).

We further compare the accuracy of our resulting 3D reconstructions against the state-of-the-art multiview technique of Nam et al. [2018]. As shown in Figure 10, our method recovers more detailed geometry, since it leverages polarization information at different angles, while Nam's work only takes into account variations in the intensity of light.

7.2 Real-World Objects

We have captured geometry and polarimetric SVBRDF of several real-world objects with our device and our sparse ellipsometry approach. Figure 11 presents results for two objects; more results with different objects are available in our supplemental material, along with videos showing different poses and dynamic illumination. The angle of linear polarization (AoLP) and the degree of polarization (DoP) are visualized as proposed by Wilkie and Weidlich [2010]. The negative components of the 3D Mueller matrices for all objects are also included in the supplemental material.

7.3 Application: Material Identification

Polarimetric appearance information may be used to identify or discriminate between materials. As an illustrative example, Figure 12 shows the results of using our sparse ellipsometry technique on a real orange and a fake one made of plastic. The first column shows the two objects, whose appearance looks almost identical. The second column shows how the single scattering component of the real fruit is significantly higher than the plastic fake, which is hollow inside. The third column shows the angle of linear polarization under linearly polarized light ($0°$). The strong single scattering in the real orange preserves the polarization of the incident light, which is not the case for the fake one.

8 DISCUSSION

Circular polarization. Our handheld setup captures four channels of linear polarization ($0°$, $45°$, $90°$, and $135°$) and illuminates with a flashlight with fixed orientation ($0°$). Therefore, the effect of circular polarization (s_3 of the Stokes vector) is not taken into account, which constitutes the main limitation of our method. Such circular polarization could be included by installing a retarder in front of the camera, but at the cost of losing one of the linear components (swapping s_2 and s_3, for instance). Another possibility would be to install and rotate optical components, which is something we avoid by design to keep our device truly portable and handheld. Furthermore, retarders have a different effect per wavelength, so using them would require additional color calibration, making our approach less practical.
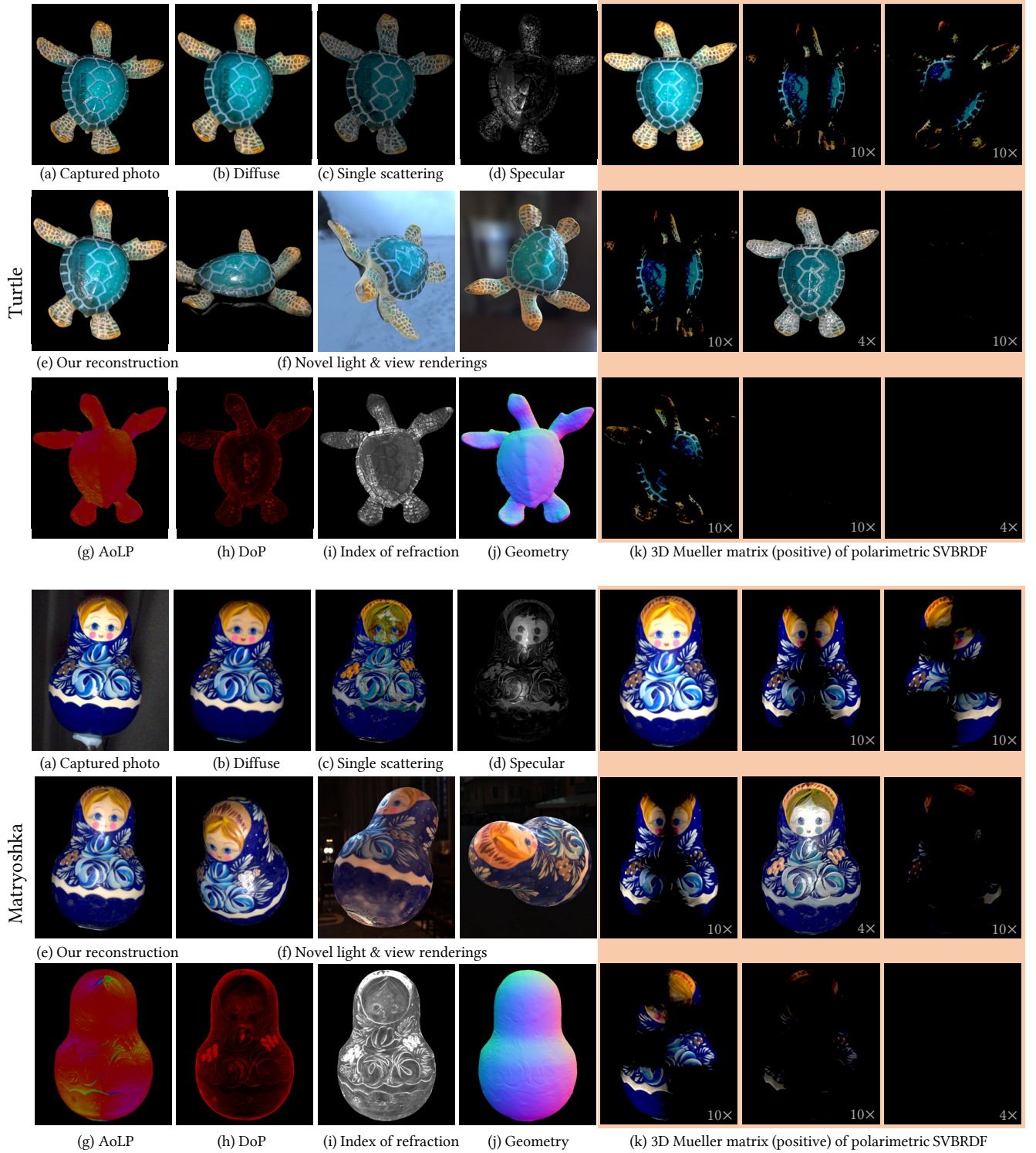
Fig. 11. Results for two examples of real objects (refer to the supplemental material for other objects and videos). (a) Captured photograph. (b) Diffuse albedo. (c) Single scattering. (d) Specular reflections. (e) Our reconstruction. (f) Novel light and view renderings. (g) Angle of linear polarization image under linearly polarized light. (h) Degree of polarization. (i) Index of refraction. (j) 3D geometry including normal information. (k) 3D Mueller matrix (positive) for a single view. Note that the non-diagonal components have been multiplied by 10, while the $M_{\{1,1\}}$ and $M_{\{2,2\}}$ components have been multiplied by 4 for visualization purposes.
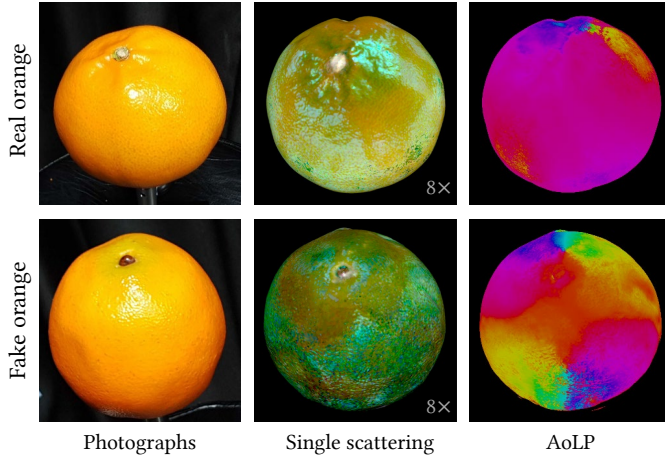
Fig. 12. Comparison of polarimetric information for a real (top) and a fake orange (bottom). Despite their similar appearance, polarimetric information allows us to distinguish between the two: the real orange presents a stronger single scattering component while preserving the polarization of incident light (as shown by the angle of linear polarization, AoLP).

Since circular polarization is omitted, our technique cannot estimate the appearance of metallic surfaces nor multiple scattering effects accurately. Nevertheless, geometry information strongly depends on linear polarization; dropping some of its components to add additional circular polarization information would lead to worse geometrical reconstructions, which would in turn lead to poor reflectance estimations. Furthermore, our polarimetric SVBRDF model is based on dielectric surfaces including Fresnel reflectance and transmittance, for which linear polarization also plays a significant role. As observed in the measured pBRDF dataset of Baek et al. [2020], the amount of circular polarization is very small in a near-coaxial setup, for a dielectric surface illuminated with linear polarization. In any case, we expect our method to degrade gracefully with increasing circular polarization.

Polarimetric SVBRDF model. An interesting finding of our optimization procedure is that the value of the single scattering roughness σ_{ss} consistently converges to a high value (> 0.9). This is to be expected in our model since σ_{ss} represents the accumulated roughness of two rough Fresnel transmissions and a phase function, so it stands to reason that it behaves as an almost diffuse lobe with specular-like orientation and polarimetry. Leveraging this, σ_{ss} could potentially be fixed to a high value during inverse rendering, saving up to an estimated 56% in computation time with no significant accuracy penalty. This strategy, while reasonable, has not been applied to any result of this paper. As a proof of concept for the owl scene, fixing $\sigma_{ss} = 1$ leads to a PSNR of 33.9 dB compared to 34.0 dB using our full pipeline while fixing $\sigma_{ss} = 0.9$ yields a PSNR of 34.2 dB.

Impact of vertex resolution and initial geometry. Vertex resolution is determined by the depth of the octree in the screened Poisson surface reconstruction method, which we set to 9. This depth provides an adequate tradeoff between geometry resolution and convergence time. Our inverse rendering method optimizes per-vertex reflectance and geometrical properties (position and normals) with small-scale

geometry shifts for mesoscale details. Similar to other state-of-the-art methods [Nam et al. 2018], our results would degrade with poor initial geometry. In all our experiments, Poisson surface reconstruction has consistently provided a good enough initial geometry, but other methods (i.e., ball pivoting or visual hull) could be used if needed.

Failure cases. While robust, our method is not free of limitations. If the captured surface is extremely dark our DoP calculation will be affected by noise, which in turn degrades the accuracy of the refractive index. Also, in situations in which the specular and single scattering components cannot be easily disambiguated (e.g., a white rough surface or a very smooth surface with dominant specularity), insufficient observations will yield imperfect separations. This may lead to dark blotches, as the single scattering image in Figure 11 (turtle scene, c) shows.

Table 2. Notations used in this paper.

	Symbol	Description
Mueller Mat. & Stokes Vec.	$\mathbf{M}$	General Mueller matrix
	$\mathbf{P}$	pBRDF, a reflectance function of (ω_i, ω_o)
	$\mathbf{P}^{d,s,ss}$	Diffuse/specular/single scattering pBRDF
	$\mathbf{C}_{i \rightarrow n}$	Coordinate conversion Mueller matrix from light to plane of incidence
	$\mathbf{C}_{n \rightarrow o}$	Coordinate conversion from plane of incidence to camera system
	$\mathbf{F}_{i,o}^T$	Incident/exitant Fresnel transmission matrix
	$\mathbf{F}^R$	Fresnel reflection matrix
	$\mathbf{D}$	depolarization matrix
	$\mathbf{s}$	General Stokes vector consisting of four elements: $[s_0, s_1, s_2, s_3]$
	$\mathbf{s}_{i,o}$	Stokes vectors of the light incident/exitant to an object surface
Geometry	$\mathbf{y}_{i,o}$	y-axis of the light/camera coordinate system
	$\mathbf{n}$	Normal vector
	ω_i	Incident light vector
	ω_o	View vector
	$\mathbf{h}$	Half way vector
	$\theta_{i,o}$	Zenith angle between normals and the incident/exitant light
	θ_h	Zenith angle between normals and halfway vector
	θ_d	Zenith angle between incident light and halfway vector
	$\phi_{i,o}$	Azimuth angle between the object plane of incidence and the y-axis of the incident/exitant
	$\varphi_{i,o}$	Azimuth angle between the micro-facet plane of incidence and the y-axis of the incident/exitant light
	$\alpha_{i,o}$	$\alpha_{i,o} = \sin(2\phi_{i,o})$
	$\beta_{i,o}$	$\beta_{i,o} = \cos(2\phi_{i,o})$
	$\chi_{i,o}$	$\chi_{i,o} = \sin(2\varphi_{i,o})$
	$\gamma_{i,o}$	$\chi_{i,o} = \cos(2\varphi_{i,o})$
Reflectance	ρ_d	Diffuse albedo
	ρ_s	Specular albedo
	ρ_{ss}	Single scattering albedo
	σ	Surface roughness
	η	Refractive index
	G	Smith's shadowing/masking function
	D	GGX micro-facet distribution function
	S	Light attenuation by shading, $S = \frac{(\mathbf{n} \cdot \omega_i)}{d^2}$
Polarization-related variables	ψ	Degree of polarization
	δ	Phase shift
	$T_i^{\perp, \parallel}$	Fresnel incident transmission coefficients
	$T_o^{\perp, \parallel}$	Fresnel exitant transmission coefficients
	$T_{i,o}^+$	$(T_{i,o}^\perp + T_{i,o}^\parallel)/2$
	$T_{i,o}^-$	$(T_{i,o}^\perp - T_{i,o}^\parallel)/2$
	$R^{\perp, \parallel}$	Fresnel reflection coefficients
	R^+	$(R^\perp + R^\parallel)/2$
	R^-	$(R^\perp - R^\parallel)/2$
	$R^\times$	$\sqrt{R^\perp R^\parallel}$

9 CONCLUSION

Our sparse ellipsometry technique allows us to estimate both shape and polarimetric SVBRDF with high accuracy, yielding results that are on par with full ellipsometry, despite needing only a few minutes (instead of days) of acquisition time, and without the need for complex tabletop capture setups. Instead, we just require a handheld camera setup with fixed polarizing optical elements, with which a series of unstructured photographs are taken. Moreover, our work overcomes the main limitations of two recent related methods that deal with polarization, lifting both the single-view constraint of Baek et al. [2018], and the single-material restriction of Baek et al. [2020], thus allowing for the first time to capture simultaneously polarimetric SVBRDF and 3D geometry. We expect that our approach will foster the development of novel accurate polarimetric imaging applications with portable devices, not limited to carefully calibrated lab conditions.

REFERENCES

Neil Alldrin, Todd Zickler, and David Kriegman. 2008. Photometric stereo with non-parametric and spatially-varying reflectance. In *Proc. IEEE Conf. Computer Vision and Pattern Recognition (CVPR) 2008*. 1–8.

Gary Atkinson and E.R. Hancock. 2006. Recovery of surface orientation from diffuse polarization. *IEEE Transactions on Image Processing* 15, 6 (jun 2006), 1653–1664. https://doi.org/10.1109/TIP.2006.871114

RMA Azzam. 1978. Photopolarimetric measurement of the Mueller matrix by Fourier analysis of a single detected signal. *Optics Letters* 2, 6 (1978), 148–150.

RMA Azzam. 2016. Stokes-vector and Mueller-matrix polarimetry. *JOSA A* 33, 7 (2016), 1396–1408.

Yunhao Ba, Alex Gilbert, Franklin Wang, Jinfa Yang, Rui Chen, Yiqin Wang, Lei Yan, Boxin Shi, and Achuta Kadambi. 2020. Deep Shape from Polarization. *Lecture Notes in Computer Science (including subseries Lecture Notes in Artificial Intelligence and Lecture Notes in Bioinformatics)* 12369 LNCS (2020), 554–571.

Seung-Hwan Baek and Felix Heide. 2021. Polarimetric Spatio-Temporal Light Transport Probing. *ACM Transactions on Graphics (Proc. SIGGRAPH Asia)* 40, 6 (2021).

Seung-Hwan Baek, Daniel S. Jeon, Xin Tong, and Min H. Kim. 2018. Simultaneous Acquisition of Polarimetric SVBRDF and Normals. *ACM Transactions on Graphics (Proc. SIGGRAPH Asia 2018)* 36, 6 (2018), 268:1–15. https://doi.org/10.1145/3272127.3275018

Seung-Hwan Baek, Tizian Zeltner, Hyun Jin Ku, Inseung Hwang, Xin Tong, Wenzel Jakob, and Min H. Kim. 2020. Image-Based Acquisition and Modeling of Polarimetric Reflectance. *ACM Transactions on Graphics (Proc. SIGGRAPH 2020)* 39, 4 (2020).

Mark Boss, Raphael Braun, Varun Jampani, Jonathan T Barron, Ce Liu, and Hendrik Lensch. 2021. Nerd: Neural reflectance decomposition from image collections. In *Proceedings of the IEEE/CVF International Conference on Computer Vision*. 12684–12694.

Guojun Chen, Yue Dong, Pieter Peers, Jiawan Zhang, and Xin Tong. 2014. Reflectance scanning: estimating shading frame and BRDF with generalized linear light sources. *ACM Transactions on Graphics (TOG)* 33, 4 (2014), 117:1–11.

Edward Collett. 2005. Field guide to polarization. Spie Bellingham, WA.

Robert L. Cook and Kenneth E. Torrance. 1982. A Reflectance Model for Computer Graphics. *ACM Transactions on Graphics (TOG)* 1, 1 (1982), 7–24. https://doi.org/10.1145/357290.357293

Zhaopeng Cui, Jinwei Gu, Boxin Shi, Ping Tan, and Jan Kautz. 2017. Polarimetric Multi-View Stereo. In *Proceedings of the IEEE Conference on Computer Vision and Pattern Recognition*. 1558–1567.

Zhaopeng Cui, Viktor Larsson, and Marc Pollefeys. 2019. Polarimetric relative pose estimation. *Proceedings of the IEEE International Conference on Computer Vision* 2019-October (2019), 2671–2680. https://doi.org/10.1109/ICCV.2019.00276

Paul E. Debevec and Jitendra Malik. 1997. Recovering High Dynamic Range Radiance Maps from Photographs. In *Proc. ACM SIGGRAPH '97*. 369–378.

Fernando del Molino and Adolfo Muñoz. 2019. Polarization mapping. *Computers & Graphics* 83 (2019), 42 – 50. https://doi.org/10.1016/j.cag.2019.06.011

Valentin Deschaintre, Yiming Lin, and Abhijeet Ghosh. 2021. Deep polarization imaging for 3D shape and SVBRDF acquisition. In *Proceedings of the IEEE/CVF Conference on Computer Vision and Pattern Recognition (CVPR)*.

Yuqi Ding, Yu Ji, Mingyuan Zhou, Sing Bing Kang, and Jinwei Ye. 2021. Polarimetric Helmholtz Stereopsis. In *2021 IEEE/CVF International Conference on Computer Vision (ICCV)*. 5017–5026. https://doi.org/10.1109/ICCV48922.2021.00499

Kenneth K Ellis. 1996. Polarimetric bidirectional reflectance distribution function of glossy coatings. *JOSA A* 13, 8 (1996), 1758–1762.

Yoshiki Fukao, Ryo Kawahara, Shohei Nobuhara, and Ko Nishino. 2021. Polarimetric Normal Stereo. In *2021 IEEE/CVF Conference on Computer Vision and Pattern Recognition (CVPR)*. 682–690. https://doi.org/10.1109/CVPR46437.2021.00074

Abhijeet Ghosh, Tongbo Chen, Pieter Peers, Cyrus A. Wilson, and Paul Debevec. 2010. Circularly polarized spherical illumination reflectometry. *ACM Transactions on Graphics* 29, 6 (2010). https://doi.org/10.1145/1866158.1866163

Abhijeet Ghosh, Graham Fyffe, Borom Tunwattanapong, Jay Busch, Xueming Yu, and Paul Debevec. 2011. Multiview face capture using polarized spherical gradient illumination. *Proceedings of the 2011 SIGGRAPH Asia Conference on - SA '11* 30, 6 (2011), 1. https://doi.org/10.1145/2024156.2024163

Abhijeet Ghosh, Tim Hawkins, Pieter Peers, Sune Frederiksen, and Paul Debevec. 2008. Practical Modeling and Acquisition of Layered Facial Reflectance. *ACM Trans. Graph.* 27, 5, Article 139 (dec 2008), 10 pages. https://doi.org/10.1145/1409060.1409092

Paulo Gotardo, Jérémy Riviere, Derek Bradley, Abhijeet Ghosh, and Thabo Beeler. 2018. Practical Dynamic Facial Appearance Modeling and Acquisition. *ACM Trans. Graph.* 37, 6, Article 232 (dec 2018), 13 pages. https://doi.org/10.1145/3272127.3275073

Pat Hanrahan and Wolfgang Krueger. 1993. Reflection from layered surfaces due to subsurface scattering. In *Proceedings of the 20th annual conference on Computer graphics and interactive techniques*. 165–174.

Eric Heitz. 2014. Understanding the Masking-Shadowing Function in Microfacet-Based BRDFs. *J. Comput. Graph. Techn.* 3, 2 (2014), 48–107.

Louis G Henyey and Jesse Leonard Greenstein. 1941. Diffuse radiation in the galaxy. *The Astrophysical Journal* 93 (1941), 70–83.

Cong Phuoc Huynh, Antonio Robles-Kelly, and Edwin R. Hancock. 2013. *Shape and refractive index from single-view spectro-polarimetric images*. Vol. 101. 64–94 pages. https://doi.org/10.1007/s11263-012-0546-3

MW Hyde IV, JD Schmidt, and MJ Havrilla. 2009. A geometrical optics polarimetric bidirectional reflectance distribution function for dielectric and metallic surfaces. *Optics express* 17, 24 (2009), 22138–22153.

Adrian Jarabo and Victor Arellano. 2017. Bidirectional Rendering of Vector Light Transport. *Computer Graphics Forum* (12 2017).

Achuta Kadambi, Vage Taamazyan, Boxin Shi, and Ramesh Raskar. 2015. Polarized 3D: High-Quality Depth Sensing with Polarization Cues. In *Proc. ICCV*. IEEE Computer Society, 3370–3378.

Christos Kampouris, Stefanos Zafeiriou, and Abhijeet Ghosh. 2018. Diffuse-Specular Separation using Binary Spherical Gradient Illumination.. In *EGSR (EI&I)*. 1–10.

Michael Kazhdan and Hugues Hoppe. 2013. Screened poisson surface reconstruction. *ACM Transactions on Graphics (TOG)* 32, 3 (2013), 29.

Jason Lawrence, Aner Ben-Artzi, Christopher DeCoro, Wojciech Matusik, Hanspeter Pfister, Ravi Ramamoorthi, and Szymon Rusinkiewicz. 2006. Inverse shade trees for non-parametric material representation and editing. *ACM Transactions on Graphics (TOG)* 25, 3 (2006), 735–745.

Joo Ho Lee, Adrian Jarabo, Daniel S. Jeon, Diego Gutierrez, and Min H. Kim. 2018. Practical Multiple Scattering for Rough Surfaces. *ACM Transactions on Graphics (TOG)* 37, 6 (2018).

Chenyang Lei, Chenyang Qi, Jiaxin Xie, Na Fan, Vladlen Koltun, and Qifeng Chen. 2021. Shape from Polarization for Complex Scenes in the Wild. (2021). arXiv:2112.11377 http://arxiv.org/abs/2112.11377

Hendrik P. A. Lensch, Jan Kautz, Michael Goesele, Wolfgang Heidrich, and Hans-Peter Seidel. 2003. Image-based Reconstruction of Spatial Appearance and Geometric Detail. *ACM Transactions on Graphics (TOG)* 22, 2 (2003), 234–257.

Fei Liu, Lei Cao, Xiaopeng Shao, Pingli Han, and Xiangli Bin. 2015. Polarimetric dehazing utilizing spatial frequency segregation of images. *Appl. Opt.* 54, 27 (Sep 2015), 8116–8122. https://doi.org/10.1364/AO.54.008116

Wan-Chun Ma, Tim Hawkins, Pieter Peers, Charles-Felix Chabert, Malte Weiss, and Paul Debevec. 2007. Rapid Acquisition of Specular and Diffuse Normal Maps from Polarized Spherical Gradient Illumination. In *Proceedings of the 18th Eurographics Conference on Rendering Techniques* (Grenoble, France) (*EGSR'07*). Eurographics Association, Goslar, DEU, 183–194.

Xiaohe Ma, Kaizhang Kang, Ruisheng Zhu, Hongzhi Wu, and Kun Zhou. 2021. Free-Form Scanning of Non-Planar Appearance with Neural Trace Photography. *ACM Trans. Graph.* 40, 4, Article 124 (jul 2021), 13 pages. https://doi.org/10.1145/3450626.3459679

JR Maxwell, J Beard, S Weiner, Da Ladd, and S Ladd. 1973. *Bidirectional Reflectance Model Validation and Utilization.* Technical Report. Environmental Research Inst Of Michiganann Arbor Infrared And Optics Div.

Ben Mildenhall, Pratul P. Srinivasan, Matthew Tancik, Jonathan T. Barron, Ravi Ramamoorthi, and Ren Ng. 2020. NeRF: Representing Scenes as Neural Radiance Fields for View Synthesis. In *ECCV*.

Daisuke Miyazaki, Robby T. Tan, Kenji Hara, and Katsushi Ikeuchi. 2003. Polarization-based inverse rendering from a single view. *Proceedings of the IEEE International Conference on Computer Vision* 2, Iccv (2003), 982–987. https://doi.org/10.1109/iccv.2003.1238455

Michal Mojzik, Tomas Skrivan, Alexander Wilkie, and Jaroslav Krivanek. 2016. Bi-Directional Polarised Light Transport. In *Eurographics Symposium on Rendering*.

Giljoo Nam, Joo Ho Lee, Diego Gutierrez, and Min H. Kim. 2018. Practical SVBRDF acquisition of 3D objects with unstructured flash photography. *ACM Transactions on Graphics* 37, 6 (2018), 1–12. https://doi.org/10.1145/3272127.3275017

Giljoo Nam, Joo Ho Lee, Hongzhi Wu, Diego Gutierrez, and Min H. Kim. 2016. Simultaneous Acquisition of Microscale Reflectance and Normals. *ACM Transactions on Graphics (Proc. SIGGRAPH Asia 2016)* 35, 6 (2016). https://doi.org/10.1145/2980179.2980220

Geoffrey Oxholm and Ko Nishino. 2014. Multiview shape and reflectance from natural illumination. *Proceedings of the IEEE Computer Society Conference on Computer Vision and Pattern Recognition* (2014), 2163–2170. https://doi.org/10.1109/CVPR.2014.277

Richard G Priest and Thomas A Gerner. 2000. *Polarimetric BRDF in the microfacet model: Theory and measurements.* Technical Report. NAVAL RESEARCH LAB WASHINGTON DC.

Jérémy Riviere, Paulo Gotardo, Derek Bradley, Abhijeet Ghosh, and Thabo Beeler. 2020. Single-Shot High-Quality Facial Geometry and Skin Appearance Capture. 39, 4 (2020). https://doi.org/10.1145/3386569.3392464

Jérémy Riviere, Ilya Reshetouski, Luka Filipi, and Abhijeet Ghosh. 2017. Polarization imaging reflectometry in the wild. *ACM Transactions on Graphics* 36, 6 (2017). https://doi.org/10.1145/3130800.3130894

Johannes L Schönberger, Enliang Zheng, Jan-Michael Frahm, and Marc Pollefeys. 2016. Pixelwise view selection for unstructured multi-view stereo. In *European Conference on Computer Vision*. Springer, 501–518.

Pratul P. Srinivasan, Boyang Deng, Xiuming Zhang, Matthew Tancik, Ben Mildenhall, and Jonathan T. Barron. 2021. NeRV: Neural Reflectance and Visibility Fields for Relighting and View Synthesis. In *CVPR*.

Yinlong Sun. 2007. Statistical ray method for deriving reflection models of rough surfaces. *JOSA A* 24, 3 (2007), 724–744.

Kenneth E Torrance and Ephraim M Sparrow. 1967. Theory for off-specular reflection from roughened surfaces. *JOSA* 57, 9 (1967), 1105–1112.

Silvia Tozza, William A.P. Smith, Dizhong Zhu, Ravi Ramamoorthi, and Edwin R. Hancock. 2017. Linear Differential Constraints for Photo-Polarimetric Height Estimation. *Proceedings of the IEEE International Conference on Computer Vision* 2017-October (2017), 2298–2306. https://doi.org/10.1109/ICCV.2017.250

Borom Tunwattanapong, Graham Fyffe, Paul Graham, Jay Busch, Xueming Yu, Abhijeet Ghosh, and Paul Debevec. 2013. Acquiring Reflectance and Shape from Continuous Spherical Harmonic Illumination. *ACM Trans. Graph.* 32, 4, Article 109 (jul 2013), 12 pages. https://doi.org/10.1145/2461912.2461944

Bruce Walter, Stephen R Marschner, Hongsong Li, and Kenneth E Torrance. 2007. Microfacet models for refraction through rough surfaces. In *Eurographics conference on Rendering Techniques*. Eurographics Association, 195–206.

Alexander Wilkie and Andrea Weidlich. 2010. A standardised polarisation visualisation for images. In *Proceedings of the 26th Spring Conference on Computer Graphics*. 43–50.

Alexander Wilkie and Andrea Weidlich. 2012. Polarised light in computer graphics. In *SIGGRAPH Asia 2012 Courses*. 1–87.

Hongzhi Wu, Zhaotian Wang, and Kun Zhou. 2016. Simultaneous Localization and Appearance Estimation with a Consumer RGB-D Camera. *IEEE Transactions on Visualization and Computer Graphics* 22, 8 (2016), 2012–2023. https://doi.org/10.1109/TVCG.2015.2498617

Hongzhi Wu and Kun Zhou. 2015. Appfusion: Interactive appearance acquisition using a kinect sensor. In *Computer Graphics Forum*, Vol. 34. Wiley Online Library, 289–298.

Rui Xia, Yue Dong, Pieter Peers, and Xin Tong. 2016. Recovering shape and spatially-varying surface reflectance under unknown illumination. *ACM Transactions on Graphics* 35, 6 (2016). https://doi.org/10.1145/2980179.2980248

Fanchao Yang, Xingjia Tang, Bingliang Hu, Ruyi Wei, Liang Kong, and Yong Li. 2016. A Method of Removing Reflected Highlight on Images Based on Polarimetric Imaging. *Journal of Sensors* 2016 (2016).

Z. Y. Zhang. 2000. A Flexible New Technique for Camera Calibration. *IEEE Trans. Pattern Analysis and Machine Intelligence* 22, 11 (Nov. 2000), 1330–1334.

Jinyu Zhao, Yusuke Monno, and Masatoshi Okutomi. 2020. Polarimetric Multi-view Inverse Rendering. *Lecture Notes in Computer Science (including subseries Lecture Notes in Artificial Intelligence and Lecture Notes in Bioinformatics)* 12369 LNCS (2020), 85–102. https://doi.org/10.1007/978-3-030-58586-0_6

Zhiming Zhou, Guojun Chen, Yue Dong, David Wipf, Yong Yu, John Snyder, and Xin Tong. 2016. Sparse-as-possible SVBRDF acquisition. *ACM Transactions on Graphics (TOG)* 35, 6 (2016), 189.

Zhenglong Zhou, Zhe Wu, and Ping Tan. 2013. Multi-view photometric stereo with spatially varying isotropic materials. *Proceedings of the IEEE Computer Society Conference on Computer Vision and Pattern Recognition* (2013), 1482–1489. https://doi.org/10.1109/CVPR.2013.195

Dizhong Zhu and William AP Smith. 2019. Depth from a polarisation + RGB stereo pair. In *Proceedings of the IEEE/CVF Conference on Computer Vision and Pattern Recognition (CVPR)*.